Original Article

Accelerated cardiac cine magnetic resonance imaging using deep low-rank plus sparse network: validation in patients

Chenyuan Yan[1#^], Yuanyuan Liu[1#], Che Wang[1], Weixiong Fan[2], Yanjie Zhu[1]

[1]Paul C. Lauterbur Research Center for Biomedical Imaging, Shenzhen Institute of Advanced Technology, Chinese Academy of Sciences, Shenzhen, China; [2]Department of Magnetic Resonance, Guangdong Provincial Key Laboratory of Precision Medicine and Clinical Translational Research of Hakka Population, Meizhou People's Hospital, Meizhou, China

Contributions: (I) Conception and design: Y Zhu; (II) Administrative support: W Fan; (III) Provision of study materials or patients: W Fan, Y Zhu; (IV) Collection and assembly of data: C Wang, C Yan; (V) Data analysis and interpretation: C Yan, Y Liu; (VI) Manuscript writing: All authors; (VII) Final approval of manuscript: All authors.

[#]These authors contributed equally to this work.

Correspondence to: Yanjie Zhu, PhD. Paul C. Lauterbur Research Center for Biomedical Imaging, Shenzhen Institute of Advanced Technology, Chinese Academy of Sciences, 1068 Xueyuan Avenue, Shenzhen University Town, Shenzhen 518055, China. Email: yj.zhu@siat.ac.cn; Weixiong Fan, MD. Department of Magnetic Resonance, Guangdong Provincial Key Laboratory of Precision Medicine and Clinical Translational Research of Hakka Population, Meizhou People's Hospital, 63 Huangtang Rd., Meizhou 514031, China. Email: fanweixiong@mzrmyy.com.

Background: Accurate and reproducible assessment of left ventricular (LV) volumes is important in managing various cardiac conditions. However, patients are required to hold their breath multiple times during data acquisition, which may result in discomfort and restrict cardiac motion, potentially compromising the accuracy of the detected results. Accelerated imaging techniques can help reduce the number of breath holds needed, potentially improving patient comfort and the reliability of the LV assessment. This study aimed to prospectively evaluate the feasibility and accuracy of LV assessment with a model-based low-rank plus sparse network (L+S-Net) for accelerated magnetic resonance (MR) cine imaging.

Methods: Fourty-one patients with different cardiac conditions were recruited in this study. Both accelerated MR cine imaging with L+S-Net and traditional electrocardiogram (ECG)-gated segmented cine were performed for each patient. Subjective image quality (IQ) score and quantitative LV volume function parameters were measured and compared between L+S-Net and traditional standards. The IQ score and LV volume measurements of cardiovascular magnetic resonance (CMR) images reconstructed by L+S-Net and standard cine were compared by paired *t*-test. The acquisition time of the two methods was also calculated.

Results: In a quantitative analysis, L+S-Net and standard cine yielded similar measurements for all parameters of LV function (ejection fraction: 35±22 for standard *vs.* 33±23 for L+S-Net), although L+S-Net had slightly lower IQ scores than standard cine CMR (4.2±0.5 for L+S-Net *vs.* 4.8±0.4 for standard cine; P<0.001). The mean acquisition time of L+S-Net and standard cine was 0.83±0.08 *vs.* 6.35±0.78 s per slice (P<0.001).

Conclusions: Assessment of LV function with L+S-Net at 3.0 T yields comparable results to the reference standard, albeit with a reduced acquisition time. This feature enhances the clinical applicability of the L+S-Net approach, helping alleviate patient discomfort and motion artifacts that may arise due to prolonged acquisition time.

Keywords: Magnetic resonance imaging (MRI); cine; deep learning (DL); cardiac function

^ ORCID: 0009-0007-9575-0742.

Submitted Jan 09, 2024. Accepted for publication Jun 03, 2024. Published online Jun 27, 2024.
doi: 10.21037/qims-24-17
View this article at: https://dx.doi.org/10.21037/qims-24-17

Introduction

Cardiovascular disease (CVD) stands as the principal cause of global mortality (1), and the diagnosis of cardiac ailments has emerged as a pivotal undertaking within global healthcare. Accurate and reproducible assessment of left ventricular (LV) volumes is important in managing various cardiac conditions, given its status as one of the most influential prognostic factors for patient outcomes (2-5). The progression of advanced cardiac diagnostic techniques is crucial for LV function assessment.

Cardiovascular magnetic resonance (CMR) imaging is recognized as the gold standard for non-invasive evaluation of biventricular volume and function. The clinical standard for data acquisition is the retrospective electrocardiogram (ECG)-gated two-dimensional (2D) segmented breath-hold (SegBH) cardiac cine imaging. This technique captures the k-space data across multiple cardiac cycles to achieve high spatial and temporal resolution. Consequently, patients are required to hold their breath multiple times during data acquisition, which may result in discomfort and restrict cardiac motion, potentially compromising the accuracy of the detected results. Furthermore, the need for multiple breath-holds may lead to hypoxemia in some patients, complicating workflow and prolonging examination duration. Fast cardiac cine imaging can significantly accelerate scan speed and allow free-breathing acquisition, simplifying the clinical examination.

Linear reconstruction methods using parallel imaging (PI), such as SENSE, and GRAPPA, have been commercially available for accelerated cine magnetic resonance imaging (MRI) (6,7). Adaptive methods such as TSENSE or TGRAPPA (8,9), allow the acquisition with a spatial and temporal resolution that shows cardiac anatomy and motion, the artifacts in the form of noise enhancement and residual aliasing can be prominent and detracted from the overall image quality (IQ), especially for acceleration rates above R=4. Methods like UNFOLD, k-t BLAST, k-t SENSE, or k-t GRAPPA (10-12), with the advantage of the spatiotemporal correlations inherent in the semiregular cardiac movement, have been shown to offer even higher acceleration rates, but are plagued by temporal blurring. Besides, the undersampled radial trajectory combined with PI, such as the radial GRAPPA method, was described and applied to accelerated real-time, free-breathing *in vivo* cardiac images (13). However, this method fails at high acceleration rates due to the assumptions that the GRAPPA weight sets must be calibrated.

Compressed sensing (CS) has also shown promise to accelerate CMR, which utilizes a non-linear algorithm to reconstruct the images from undersampled k-space data with sparse representations of the cine images (14). Sparse transforms such as temporal frequency, spatial wavelet, and spatiotemporal finite difference have been previously explored (15,16). Instead of using a single sparsity constraint, adaptive methods relying on transforms derived from the data itself, such as k-t PCA, k-t SLR, LLR, LOST, blind CS, which exploit sparsity and low-rank structure of the image matrix, were then proposed (17-20). They all enforce a global model on every time profile being expressed as a combination of a few temporal basis functions. These basis functions can be orthogonal (e.g., estimated using singular value decomposition), or non-orthogonal (e.g., estimated via dictionary learning) (21,22). Among these methods, a CS-based method using the low-rank plus sparse (L+S) decomposition model has been recently proposed to accelerate the CMR acquisition. It decomposes an observation matrix X into the sum of a low-rank component L and a sparse component S. L captures the highly correlated background common to temporal frames. S models sparsely distribute dynamic changes between frames. This decomposition naturally fits dynamic MRI where the background is slowly varying and dynamics appear locally. To recover X from undersampled measurements, L+S reconstruction formulates an optimization problem that minimizes the nuclear norm of L and l_1-norm of S, subject to data consistency constraints. By separately modeling background and dynamics, L+S has been shown to better compress dynamic image series than low-rank reconstruction alone. This enables higher acceleration and improved reconstruction of highly undersampled dynamic MRI datasets.

Generally, the acceleration rate of linear reconstruction methods is limited, as it relies on the fixed architecture of the receiver coil array and the associated g-factor signal-to-noise ratio (SNR) losses, which restricts the achievable acceleration factors. In contrast, CS-based methods

suffer from long reconstruction time due to the iterative reconstruction process, and can only be used for random undersampling patterns, which do not support equispaced acceleration as effectively as PI techniques.

In recent years, deep learning (DL)-based methods have become increasingly popular in image reconstruction and shown great potential in significantly speeding up MRI (23,24). DL-based methods can complete the reconstruction within seconds for a new scan, overcoming the issue of CS reconstructions that require prolonged computation time. Therefore, they are more suited for clinical scenarios and time-sensitive imaging scans. Generally speaking, two main categories of DL methods have been explored: unsupervised learning and supervised learning. Unsupervised learning methods aim to train the networks without fully sampled k-space data. They either learn the probability distribution of images by network and enforce this network-based image prior as an explicit constraint into the image reconstruction framework (25-27) or use the sampled data to train the networks (28,29). Supervised learning methods typically require training pairs to train the network in an end-to-end fashion during the training stage. There are roughly two types of supervised learning methods: unrolling-based methods and those not based on unrolling. One type of supervised learning method leverages a vanilla network to learn a mapping from undersampled data to the fully sampled versions. The architectures commonly used in MR image reconstruction are fully connected (FC) (30), convolutional neural network (CNN) (31-33), multi-layer perceptron (MLP) (34), U-Net (a type of CNN) (35-37), and generative adversarial network (GAN) (38-40). The second type of supervised learning method utilizes the unrolling-based methods networks for accelerated cardiac cine MRI. The unrolling-based methods networks (also referred to as physics-guided DL reconstruction) unroll the existing iterative reconstruction algorithms to deep networks in which the hyper-parameters and regularizations can be learned through network training (41-48). Unrolled networks leverage the structure of iterative optimization algorithms and integrate them into deep neural network architectures, enabling efficient and interpretable reconstruction. Examples of unrolled network approaches include iterative shrinkage-thresholding algorithm-network (ISTA-Net), Cine-net, MoDL, ADMM-Net, variational networks, and deep cascade networks (41,42,47-50). For example, ISTA-Net employs the unrolling-based framework to solve CS reconstruction models (50). It outperforms existing state-of-the-art optimization-based CS methods and maintains fast computational speed (50). Cheng *et al.* proposed a DL network to implicitly learn the data consistency in accordance with the underlying probability distribution of system noise (referred to as learned data consistency network) (51). The efficacy of this approach has been demonstrated in dynamic imaging applications.

Recently, an unrolled network, known as low-rank plus sparse network (L+S-Net), has been proposed by Huang *et al.* (52). It exhibits strong interpretability and delivers high-quality images. However, this approach has not yet been optimized or prospectively evaluated in a clinical setting. The purpose of this study was to prospectively validate the performance of the highly accelerated cardiac cine imaging with L+S-Net in clinical scenarios. The conventional segmented balanced steady-state free precession (bSSFP) was used as the reference standard. We present this article in accordance with the STROBE reporting checklist (available at https://qims.amegroups.com/article/view/10.21037/qims-24-17/rc).

Methods

The study was conducted in consistent with the Declaration of Helsinki (as revised in 2013). It was approved by the Ethics Committee at the Shenzhen Institute of Advanced Technology, Chinese Academy of Sciences (No. YSB-2022-Y07066), and written informed consent was obtained from all participants.

Accelerated cine sequence and DL reconstruction

A two-dimensional (2D) bSSFP sequence was implemented for the accelerated cine acquisition using an undersampling pattern in phase-encoding and temporal dimensions with a net acceleration rate of 14.2. The variable spatial-temporal Latin hypercube and echo-sharing sampling scheme (VALAS) (53) was employed for the undersampling pattern of the bSSFP sequence, with the center k-space 4-fold accelerated, transition region 6-fold accelerated, and outer region 14-fold accelerated (*Figure 1*). This VALAS sampling scheme has less statistical fluctuation along time direction than the traditional variable density random sampling, and may achieve better IQ and temporal profile (54). The frequency encoding direction was fully sampled, while the undersampling was applied in the phase encoding direction.

Figure 1 illustrates the framework of the L+S-Net employed to reconstruct the accelerated cine MRI data.

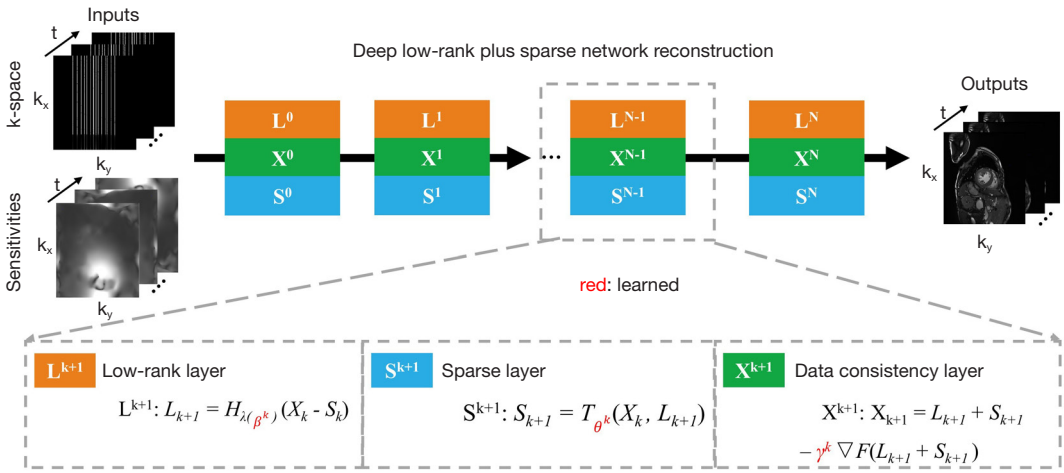

Figure 1 The framework of L+S-Net for accelerated MR cine imaging. The sampling mask in the k_y-t direction used in the VALAS method is shown as an example. L+S-Net, low-rank plus sparse network; MR, magnetic resonance; VALAS, variable spatial-temporal Latin hypercube and echo-sharing sampling scheme.

The network used was the same as that described by Huang *et al.* (52). The L+S-Net is an unrolled deep-learning network based on the L+S method (55). First, the dynamic MR image is formulated as a low-rank plus sparse model under the CS framework. It can be solved using an alternating linearized minimization method to recover the low-rank (L) and sparse (S) components iteratively. Then, this complex iterative procedure is unrolled into an N-block network using the following equation, with each block representing an iteration and N being a relatively small integer:

$$\begin{cases} L^{k+1}: & L_{k+1} = H_{\lambda(\beta^k)}\left(X_k - S_k\right) \\ S^{k+1}: & S_{k+1} = \mathcal{T}_{\theta^k}\left(X_k, L_{k+1}\right) \\ X^{k+1}: & X_{k+1} = L_{k+1} + S_{k+1} - \gamma^k \nabla F\left(L_{k+1} + S_{k+1}\right) \end{cases} \quad [1]$$

where L_k, S_k, X_k represents the low-rank prior layer, sparse prior layer, and data consistency layer, respectively. $H_{\lambda(\beta^k)}$ represents the learned singular value thresholding (LSVT) operator which forces the matrix to be low-rank by eliminating small singular values with a threshold of $\lambda(\beta^k)$. $\mathcal{T}_{\theta^k}$ is a residual 3D CNN used to learn a customized proximal operator for each unrolling block. θ^k is the set of CNN parameters. γ^k is the learnable update step size for the kth iteration block. $\nabla F(\cdot)$ represents the gradient of the data fidelity term $F(\cdot)$. More details can be found in the work proposed by Huang *et al.* (52). All the regularization parameters are designated as learnable in the L+S-Net, encompassing the LSVT, the update step size, and the proximal operator, eliminating the need for empirical selection. The network inputs are the undersampled k-space data and the corresponding coil sensitivity maps estimated using ESPIRiT implemented in BART (56).

The L+S-Net was implemented in Tensor Flow2.2, using an exponentially decayed learning rate during the training process. The initial learning rate is set to 0.001, and the attenuation coefficient is set to 0.95. The model is trained by the Adam optimizer.

Study population

Three cardiac cine datasets were used in this work, two for the training dataset and test dataset in the retrospective study, and the third one for the prospective study.

Training dataset for the retrospective study

The training data were the fully sampled cine data acquired from 29 healthy volunteers on a 3T scanner (MAGNETOM Trio, Siemens Healthcare, Erlangen, Germany) with a multichannel receiver coil array (20 coils), corresponding to a total of 386 cardiac slices. All *in vivo* experiments were conducted with IRB approval and informed consent. For each subject, 10 to 13 short-axis slices were imaged with the retrospective ECG-gated segmented bSSFP sequence during breath holding, with a field of view (FOV) of 330×330 mm, acquisition matrix of 256×256, slice thickness of 6 mm, repetition time (TR)/echo time (TE) of 3.0 ms/1.5 ms. The acquired temporal resolution was

Table 1 Summary of study population and cardiac MRI characteristics (n=41)

Variable	Value
Sex (female/male)	13/28
Age (years)	52.4±17.5
Height (cm)	162.3±6.4
Weight (kg)	62.4±14.0
BMI (kg/m^2)	23.4±4.9
Heart rate (bpm)	77.3±10.9
Cardiovascular disease	
Dilated cardiomyopathy	12
Hypertensive heart disease	2
Cardiomegaly	2
AMI	2
Heart failure	2
Myocarditis	3
SLE cardiomyopathy	1
ACS	1
Chest pain	1
Other	15

Data are presented as mean ± standard deviation and number. MRI, magnetic resonance imaging; BMI, body mass index; bpm, beats per minutes; AMI, acute myocardial infarction; SLE, systemic lupus erythematosus; ACS, acute coronary syndrome.

40.0 ms, and each data point had approximately 25 phases that covered the entire cardiac cycle. To augment the dataset for DL training, we applied stride and cropping to the dynamic images, sliding a 192×192×18 (x×y×t) box with a stride of 25, 25, and 7 along the x, y, and t directions, respectively.

Testing data for the retrospective study

To test the performance of the L+S-Net, fully sampled cine data were acquired from 5 healthy volunteers on a 3T MR scanner (uMR790, United Imaging, Shanghai, China) with 24 channels in our local institute. During breath-holding, each subject imaged 10 to 12 short axis slices with retrospective ECG gated segmented bSSFP sequence. The readout direction resolution is 256 and the phase coding resolution is 226, with a FOV of 384×339 mm, slice thickness of 8 mm, and TR/TE of 3.2 ms/1.5 ms. The acquired temporal resolution was 40.0 ms. The testing data were retrospectively undersampled with the predefined undersampling mask and reconstructed with the L+S-Net. The fully sampled images served as the references. We also compared the results of L+S-Net with those using the L+S method, as well as state-of-the-art DL-based reconstruction methods, such as ISTA-Net and learned data consistency network (DC-Net).

Testing data for the prospective study

To prospectively validate the L+S-Net, 41 patients (28 male, age: 52±17 years; 13 female, age: 53±20 years) with different cardiac conditions were recruited at a single tertiary hospital from May 2022 through May 2023. Inclusion criteria were patients clinically scheduled for CMR assessment. Exclusion criteria included general contraindications to MRI (e.g., cardiac implantable electronic device and claustrophobia) or refusal to participate. The details of the patient population are summarized in *Table 1*.

CMR acquisitions were performed on clinical 3T MR scanners (either uMR780 or uMR890, United Imaging, Shanghai, China) with a 24-channel cardiac coil. The parameters of accelerated cine imaging were: FOV =320×360 mm; slice thickness =8 mm; matrix size =192×210; flip angle =45°; TE/TR =1.29/2.78 ms; temporal resolution =37.6 ms; acceleration factor =14.2; 8–12 short axis slices were acquired depending on the heart size of participants. The average acquisition time was 6.70±0.30 s for the whole heart (0.83±0.08 s per slice). Standard cine was also acquired using the segmented bSSFP sequence at the same locations as the accelerated cine with the following parameters: FOV =320×360 mm; slice thickness =8 mm; matrix size =199×224; flip angle =45°; TE/TR =1.29/2.76 ms. The acquisitions for the accelerated cine were performed under breath-hold conditions and prospective ECG triggering. Breath-holding is primarily to obtain a more accurate quantitative cardiac function assessment. For patients who cannot tolerate breath-holding, free-breathing acquisition can also be performed. The average acquisition time was 176.00±18.46 s including the resting time between the successive acquisitions, (6.35±0.78 s per slice).

IQ assessment

For retrospectively undersampled data, the IQ was assessed using two metrics: peak signal-to-noise ratio (PSNR) and structural similarity index measure (SSIM). PSNR indicates the PSNR of an image, with the fully sampled image as the reference, while SSIM represents the structural

Table 2 Image quality scoring criteria for cardiac cine

Score	Overall image quality criteria
1	Nondiagnostic—evident motion-related artifacts or distortions, with poor contrast and clarity
2	Fair—obvious motion-related artifacts or image distortion are present. The contrast and clarity are below par
3	Adequate—moderate motion-related artifacts or image distortion. The contrast and clarity are average but still sufficient to depict the ventricular outline without affecting clinical diagnosis
4	Good—mild motion-related artifacts or image distortion with good contrast and clarity
5	Excellent—minimal to no motion-related artifacts or image distortion with excellent contrast and clarity

similarity index for a grayscale image relative to the fully sampled image. Furthermore, an evaluation metric for image blurring, which relies on the maximum gradient and gradient variability, was employed (57).

For the prospective study, two radiologists (7 and 4 years of CMR experience, respectively) assessed images of the two cine sequences independently, focusing on the myocardial border and artifacts. General IQ was evaluated visually using a European five-point Likert scale: 5 = excellent IQ, 4 = normal IQ, 3 = presence of artifacts but sufficient IQ, 2 = severe artifacts around ventricles, and 1 = completely non-diagnostic images. The scoring criteria are listed in *Table 2*.

Quantitative measurements of cardiac function were performed using the cardiac analysis software Segment v4.0 R11044c (Academic Research only version) (https://medviso.com/). Six quantitative values were measured, including end-diastolic volume (EDV), end-systolic volume (ESV), stroke volume (SV), LV mass (LVM), LV ejection fraction (LVEF), and cardiac output (CO).

Statistical analysis

For retrospectively undersampled data, we have conducted statistical hypothesis tests to demonstrate the significance of two indicators (PSNR and SSIM) for L+S-Net, DC-Net, ISTA-Net, and L+S. None of the indicators (PSNR and SSIM) for L+S-Net, DC-Net, ISTA-Net, and L+S, except for the SSIM of L+S-Net, followed a normal distribution. Therefore, we used quartiles to describe the distribution of both SSIM and PSNR metrics and conducted Wilcoxon Signed Ranks tests.

For prospectively accelerated cine, the IQ scores were compared using the paired *t*-test. The LV function of CMR images reconstructed by L+S-Net and standard cine was also quantified and compared by paired *t*-test. Bland-Altman analysis was used to evaluate the agreement of quantitative LV function parameters between different techniques. A P value <0.05 was considered statistically significant. All statistical analyses were performed with IBM SPSS Statistics 25 software.

Results

Retrospective experiment

Figure 2 shows the reconstructed images of L+S-Net, L+S, ISTA-Net, and DC-Net methods, along with the reference images from fully sampled data. The rows represent the diastole and systole cardiac phases of the same subject. PSNR and SSIM values are shown in the left corners. The y-t image (extraction of the 92nd slice along the y and temporal dimensions) is also given to show the reconstruction performance in the temporal dimension. The L+S-Net demonstrates the highest SSIM score among the four methods. From the y-t view, the L+S-Net captures the dynamic information comparable to the reference. Compared with the DL-based methods, the CS-based L+S method visually shows the most blurry reconstructions and obvious stripes can be observed in the y-t image, which may indicate the artifacts in the reconstructed images. In terms of PSNR and SSIM, L+S-Net and DC-Net had similar values, both outperforming ISTA-Net. The values of blurring assessment for the L+S-Net, L+S, ISTA-Net, and DC-Net are 2.1050, 2.1965, 2.1836, and 2.1107, respectively. In terms of the blurring metric, the L+S-Net shows a value closest to the reference value of 2.0456 among the four methods. This comparative blurring analysis result reveals the superiority of the L+S-Net in preserving image sharpness (57).

Figure 3 presents the statistical results of PSNR and SSIM among the three DL-based methods and the L+S method. Similar to *Figure 2*, the reconstructions of the L+S method show the lowest PSNR and SSIM. L+S-Net demonstrates the highest SSIM score with statistical significance (P<0.05). Specifically, the PSNR of L+S-Net was compared to the L+S method, ISTA-Net, and DC-Net using statistical tests. The P value for the comparison between L+S-Net and the L+S method was P<0.001, while

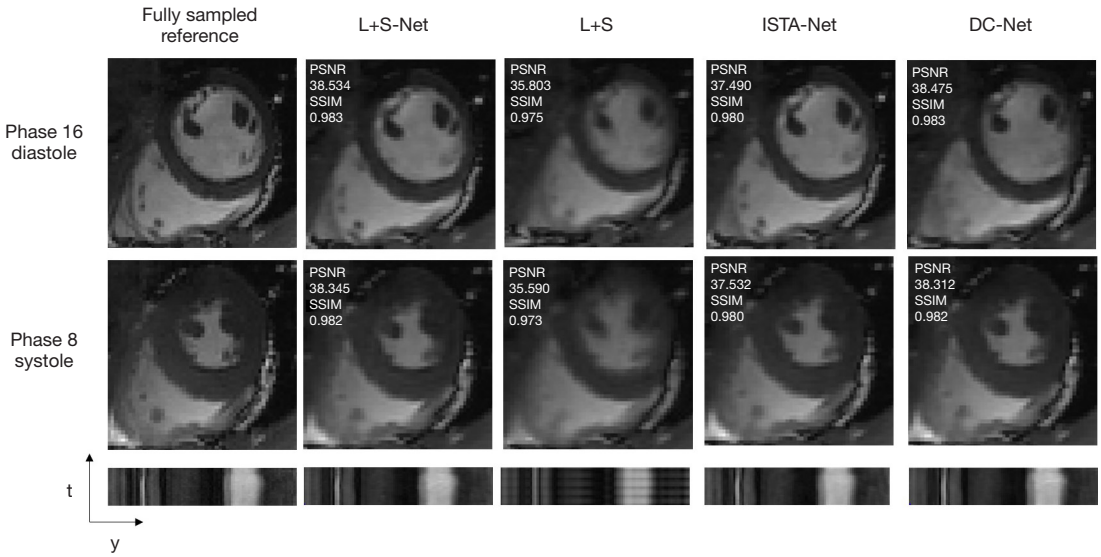

Figure 2 Reconstruction results for a single subject at end-diastole and end-systole using the L+S-Net, L+S, ISTA-Net, and DC-Net approaches. The first row displays the images of the cardiac diastolic phase, the second row shows the images of the cardiac systolic phase of the same subject, and the third row presents the y-t view. The y-t images (extraction of the 92nd slice along the y and temporal dimensions) demonstrate the reconstruction performance in the temporal dimension. L+S-Net, low-rank plus sparse network; L+S, low-rank plus sparse; ISTA-Net, iterative shrinkage-thresholding algorithm network; DC-Net, learned data consistency network; PSNR, peak signal-to-noise ratio; SSIM, structural similarity index measure.

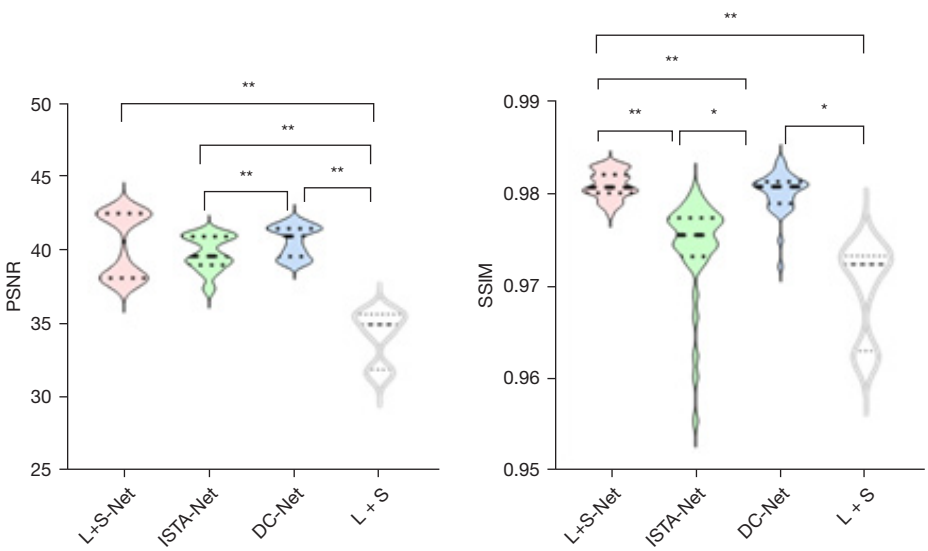

Figure 3 Comparisons of different methods for the retrospective reconstructions. PSNR: DC-Net > ISTA-Net > L+S, L+S-Net > L+S; SSIM: L+S-Net > DC-Net > ISTA-Net > L+S. *, P<0.05; **, P<0.001. L+S-Net, low-rank plus sparse network; ISTA-Net, iterative shrinkage-thresholding algorithm network; DC-Net, learned data consistency network; L+S, low-rank plus sparse; PSNR, peak signal-to-noise ratio; SSIM, structural similarity index measure.

Table 3 Training time and average reconstruction time for different methods

Method	Training time (s)	Average reconstruction time (s)
L+S-Net	93,465.5	1.5
L+S	Not available	112.6
ISTA-Net	49,502.5	1.0
DC-Net	252,692.2	1.4

Data are presented as mean. L+S-Net, low-rank plus sparse network; L+S, low-rank plus sparse; ISTA-Net, iterative shrinkage-thresholding algorithm network; DC-Net, learned data consistency network.

Table 4 LV volume measurements between standard cine and L+S-Net

Parameters	Standard cine	L+S-Net	P
LVM	121±49	122±51	0.891
EDV	190±93	175±86	0.467
ESV	139±101	131±95	0.730
SV	51±22	44±23	0.188
EF	35±22	33±23	0. 685
CO	3.8±1.4	3.3±1.5	0.091

Data are presented as mean ± standard deviation. LV, left ventricular; L+S-Net, low-rank plus sparse network; LVM, left ventricular mass; EDV, end-diastolic volume; ESV, end-systolic volume; SV, stroke volume; EF, ejection fraction; CO, cardiac output.

the comparisons between L+S-Net and ISTA-Net, and L+S-Net and DC-Net, yielded P values of 0.055 and 0.136, respectively, neither of which were statistically significant.

Table 3 shows the training and average reconstruction times for each technique. The training times for L+S-Net, ISTA-Net, and DC-Net were 93,465.5, 49,502.5, and 252,692.2 s, respectively. The average reconstruction times for L+S-Net, L+S, ISTA-Net, and DC-Net were 1.5, 112.6, 1.0, and 1.4 s, respectively.

Prospective experiment

Standard cine CMR images served as the reference standard for measuring LV function. Six metrics were measured, including LVM, EDV, ESV, SV, EF and CO. *Table 4* displays the analysis results of the LV function of the standard cine and L+S-Net. There were no significant differences between standard cine and L+S-Net for any of the LV function metrics.

The Bland-Altman plots revealed no significant differences for the L+S-Net and standard cine concerning corresponding LVM, EDV, ESV, SV, EF, and CO (shown in *Figure 4*). The mean differences of parameters are as follows: LVM, bias: 3.1, 95% CI: −16.0 to 22.3; EDV, bias: −9.8, 95% CI: −41.5 to 21.9; ESV, bias: −2.6, 95% CI: −34.7 to 29.5; SV, bias: −7.0, 95% CI: −24.2 to 10.1; EF, bias: −2.4, 95% CI: −16.1 to 11.3; CO, bias: −0.6, 95% CI: −1.8 to 0.7. The Bland-Altman plots revealed acceptable agreement for the L+S-Net and standard cine concerning corresponding LVM, EDV, ESV, SV, EF, and CO.

Figure 5 shows representative images of standard cine and L+S-Net from four patients. All images showed adequate diagnostic IQ. A contrast difference can be observed between images of the standard cine and L+S-Net for patient 3. It may result from the intensity inhomogeneity caused by the B1 inhomogeneity and the spatial inhomogeneity of coil sensitivity of surface coils during the acquisition. Since the images of standard cine were obtained from the MRI scan system with intensity inhomogeneity correction, the reconstructions of L+S-Net haven't undergone this process.

Figure 6 shows the stacked bar plot of the distribution of IQ ratings of the reconstructions of the L+S-Net and the standard cine. The L+S-Net yielded slightly worse IQ scores than standard cine CMR (4.2±0.5 for L+S-Net *vs.* 4.8±0.4 for standard cine; P<0.001), which further confirms that the L+S-Net can achieve clinically acceptable reconstructions.

Discussion

In the retrospective study, L+S-Net performed excellently in terms of PSNR and SSIM compared to DC-Net, ISTA-Net, and L+S method. As shown by Huang *et al.* (52), L+S-Net exhibits better performance in detail reconstruction and contrast, resulting in lower errors in edge and high-frequency regions, indicating the importance of the low-rank and sparse prior. While L+S-Net outperformed the other methods in terms of SSIM, the differences in PSNR were not as dramatic. PSNR is a SNR-based metric that is sensitive to overall image fidelity, whereas SSIM focuses more on perceptual similarity. The lack of statistical significance in the PSNR differences between L+S-Net and the other methods could be attributed to the inherent

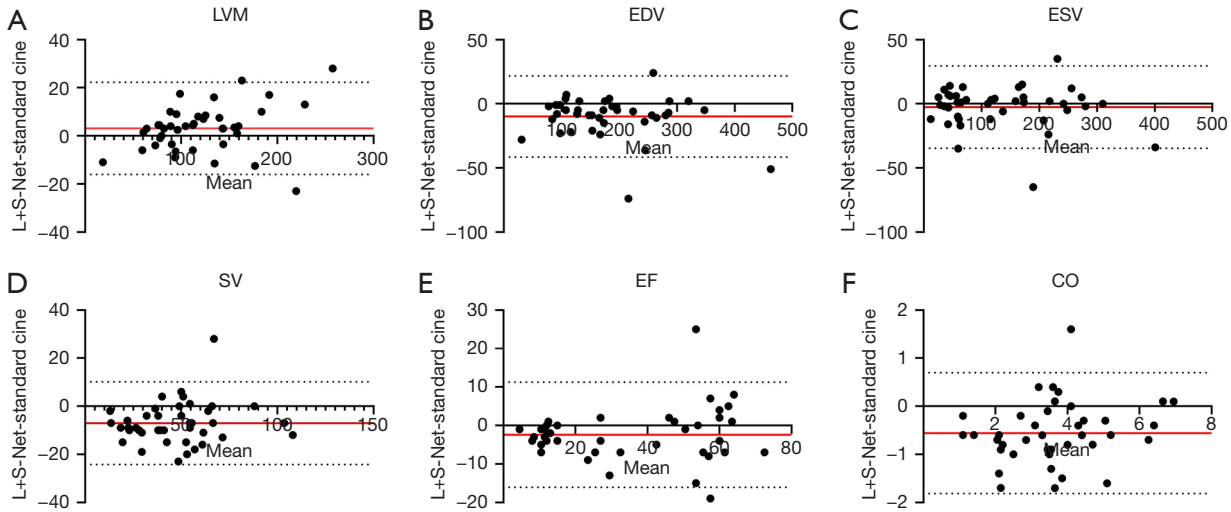

Figure 4 Bland-Altman plots applied to evaluate LV functional parameters including (A) LVM, (B) EDV, (C) ESV, (D) SV, (E) EF and (F) CO. Mean differences between L+S-Net techniques and standard cine. The solid line indicates the bias between the two techniques; the dashed lines indicate the 95% limits of agreement interval (i.e., the bias ±1.96 SD). L+S-Net, low-rank plus sparse network; LVM, left ventricular mass; EDV, end-diastolic volume; ESV, end-systolic volume; SV, stroke volume; EF, ejection fraction; CO, cardiac output; SD, standard deviation.

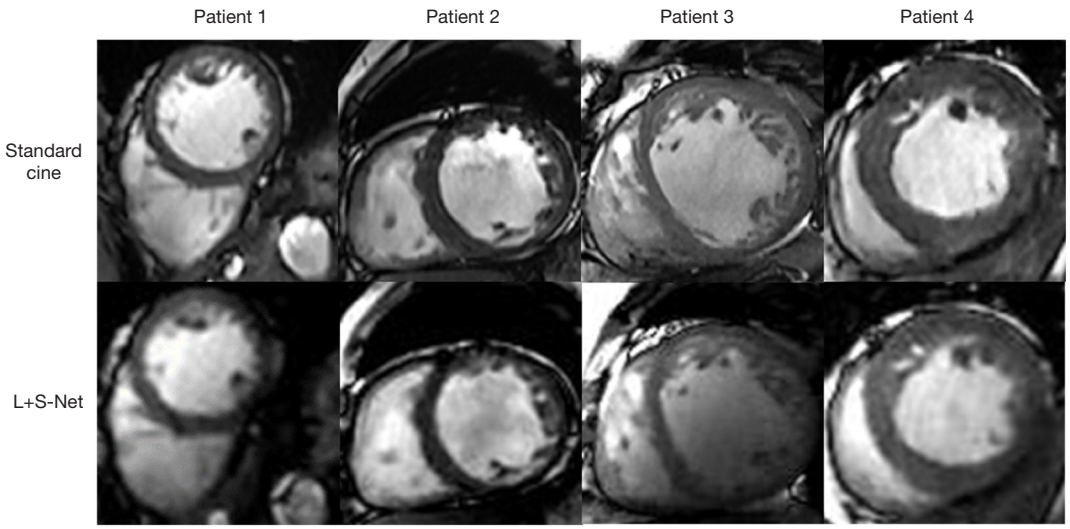

Figure 5 Case examples show the diagnostic image quality of standard cine and L+S-Net. L+S-Net, low-rank plus sparse network.

trade-offs between different quality metrics. L+S-Net may have prioritized preserving structural and textural details, leading to superior SSIM performance, while the PSNR scores were more comparable to the other approaches. In the prospective study, L+S-Net showed high agreement for the volumetric analysis of the left ventricle, compared to the standard cine CMR. The quality scores for all images exceeded a value of 3, indicating their adequacy. This outcome implies that the L+S-Net is capable of producing images of satisfactory diagnostic quality.

In previous studies, the subjective IQ scores of DL-based cine techniques were consistently lower than conventional methods, which is consistent with our results (58-62). As demonstrated by the case examples in our study, there were

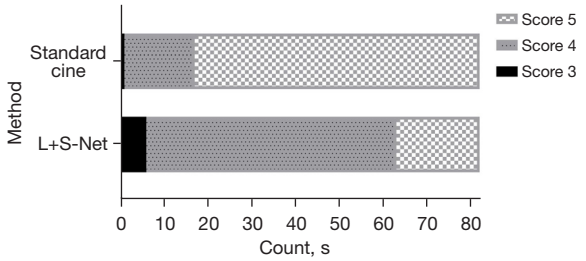

Figure 6 Stacked bar plot showing the distribution of image quality ratings: L+S-Net *vs.* standard cine CMR. L+S-Net, low-rank plus sparse network; CMR, cardiovascular magnetic resonance.

noticeable differences in image contrast and clarity with the L+S-Net, most likely attributable to undersampling and the image reconstruction process. This likely contributed to the marginally lower IQ scores when compared to the reference standard. With further refinement, especially in addressing the disparities in image contrast and clarity, the L+S-Net demonstrates significant potential for enabling swifter data acquisitions for quantitative analysis. This could lead to less burdensome examinations for patients requiring such assessments.

In a quantitative analysis, L+S-Net and standard cine yielded similar measurements for all parameters of LV function. Many studies demonstrated strong agreement in quantitative measurements between DL-based cine techniques and traditional techniques, although statistically significant differences were still observed in some parameters. These variations are inconsistent across different studies. Kido *et al.* (62) used CS real-time cine sequence for LV analysis in healthy controls and patients. They demonstrated CS real-time cine accurately measured RV volumetry. Zucker *et al.* (61) assessed the IQ and performance of a DL-based cine sequence reconstruction compared with reference standard bSSFP. There were small but statistically significant volumetric differences between DL-based cine and the reference bSSFP cine for LVEF and RVEF. Yan *et al.* (58) applied CS-cine and AI-cine sequences to evaluate biventricular cardiac function analysis in a patient cohort at 3.0 T. Compared with conventional segmented, retrospectively gated cine, the CS-cine and AI-cine yielded similar LVESV, LVEF, RVEDV, RVESV, and RVEF but slightly smaller and statistically significant LVEDV. Our results did not show LVEDV underestimation, perhaps because with the low-rank and sparse prior, L+S-Net exhibits better performance in detail reconstruction and contrast, which leads to a lower error level around edges and high-frequency areas.

Conclusions

In conclusion, L+S-Net is proved to be a promising method for cardiac cine imaging in a clinical setting and it yields good IQ and highly accurate volumetric and functional measures relative to standard segmented cine acquisition.

Acknowledgments

Funding: This work was funded by the National Key R&D Program (Nos. 2021YFF0501402, 2020YFA0712200, and 2023YFA1011403), the National Natural Science Foundation of China (Nos. 62322119, 62201561, 12226008, 81971611, and U21A6005), the Guangdong Basic and Applied Basic Research Foundation (No. 2021A1515110540), the Key Laboratory for Magnetic Resonance and Multimodality Imaging of Guangdong Province (No. 2023B1212060052), and Shenzhen Science and Technology (Nos. RCYX20210609104444089 and JCYJ20220818101205012).

Footnote

Reporting Checklist: The authors have completed the STROBE reporting checklist. Available at https://qims.amegroups.com/article/view/10.21037/qims-24-17/rc

Conflicts of Interest: All authors have completed the ICMJE uniform disclosure form (available at https://qims.amegroups.com/article/view/10.21037/qims-24-17/coif). The authors have no conflicts of interest to declare.

Ethical Statement: The authors are accountable for all aspects of the work in ensuring that questions related to the accuracy or integrity of any part of the work are appropriately investigated and resolved. The study was conducted in consistent with the Declaration of Helsinki (as revised in 2013). It was approved by the Ethics Committee at the Shenzhen Institute of Advanced Technology, Chinese Academy of Sciences (No. YSB-2022-Y07066), and written informed consent was obtained from all participants.

References

1. Global, regional, and national burden of chronic kidney disease, 1990-2017: a systematic analysis for the Global Burden of Disease Study 2017. Lancet 2020;395:709-33.
2. Shah S, Segar MW, Kondamudi N, Ayers C, Chandra A, Matulevicius S, Agusala K, Peshock R, Abbara S, Michos ED, Drazner MH, Lima JAC, Longstreth WT Jr, Pandey A. Supranormal Left Ventricular Ejection Fraction, Stroke Volume, and Cardiovascular Risk: Findings From Population-Based Cohort Studies. JACC Heart Fail 2022;10:583-94.
3. He J, Yang W, Wu W, Li S, Yin G, Zhuang B, Xu J, Sun X, Zhou D, Wei B, Sirajuddin A, Teng Z, Zhao S, Kureshi F, Lu M. Early Diastolic Longitudinal Strain Rate at MRI and Outcomes in Heart Failure with Preserved Ejection Fraction. Radiology 2021;301:582-92.
4. Li S, Wang Y, Yang W, Zhou D, Zhuang B, Xu J, He J, Yin G, Fan X, Wu W, Sharma P, Sirajuddin A, Arai AE, Zhao S, Lu M. Cardiac MRI Risk Stratification for Dilated Cardiomyopathy with Left Ventricular Ejection Fraction of 35% or Higher. Radiology 2023;306:e213059.
5. Houbois CP, Nolan M, Somerset E, Shalmon T, Esmaeilzadeh M, Lamacie MM, Amir E, Brezden-Masley C, Koch CA, Thevakumaran Y, Yan AT, Marwick TH, Wintersperger BJ, Thavendiranathan P. Serial Cardiovascular Magnetic Resonance Strain Measurements to Identify Cardiotoxicity in Breast Cancer: Comparison With Echocardiography. JACC Cardiovasc Imaging 2021;14:962-74.
6. Griswold MA, Jakob PM, Heidemann RM, Nittka M, Jellus V, Wang J, Kiefer B, Haase A. Generalized autocalibrating partially parallel acquisitions (GRAPPA). Magn Reson Med 2002;47:1202-10.
7. Pruessmann KP, Weiger M, Boesiger P. Sensitivity encoded cardiac MRI. J Cardiovasc Magn Reson 2001;3:1-9.
8. Breuer FA, Kellman P, Griswold MA, Jakob PM. Dynamic autocalibrated parallel imaging using temporal GRAPPA (TGRAPPA). Magn Reson Med 2005;53:981-5.
9. Kellman P, Epstein FH, McVeigh ER. Adaptive sensitivity encoding incorporating temporal filtering (TSENSE). Magn Reson Med 2001;45:846-52.
10. Guttman MA, Kellman P, Dick AJ, Lederman RJ, McVeigh ER. Real-time accelerated interactive MRI with adaptive TSENSE and UNFOLD. Magn Reson Med 2003;50:315-21.
11. Huang F, Akao J, Vijayakumar S, Duensing GR, Limkeman M. k-t GRAPPA: a k-space implementation for dynamic MRI with high reduction factor. Magn Reson Med 2005;54:1172-84.
12. Tsao J, Kozerke S, Boesiger P, Pruessmann KP. Optimizing spatiotemporal sampling for k-t BLAST and k-t SENSE: application to high-resolution real-time cardiac steady-state free precession. Magn Reson Med 2005;53:1372-82.
13. Seiberlich N, Ehses P, Duerk J, Gilkeson R, Griswold M. Improved radial GRAPPA calibration for real-time free-breathing cardiac imaging. Magn Reson Med 2011;65:492-505.
14. Lustig M, Donoho D, Pauly JM. Sparse MRI: The application of compressed sensing for rapid MR imaging. Magn Reson Med 2007;58:1182-95.
15. Jung H, Ye JC, Kim EY. Improved k-t BLAST and k-t SENSE using FOCUSS. Phys Med Biol 2007;52:3201-26.
16. Otazo R, Kim D, Axel L, Sodickson DK. Combination of compressed sensing and parallel imaging for highly accelerated first-pass cardiac perfusion MRI. Magn Reson Med 2010;64:767-76.
17. Gamper U, Boesiger P, Kozerke S. Compressed sensing in dynamic MRI. Magn Reson Med 2008;59:365-73.
18. Lingala SG, Hu Y, DiBella E, Jacob M. Accelerated dynamic MRI exploiting sparsity and low-rank structure: k-t SLR. IEEE Trans Med Imaging 2011;30:1042-54.
19. Shin PJ, Larson PE, Ohliger MA, Elad M, Pauly JM, Vigneron DB, Lustig M. Calibrationless parallel imaging reconstruction based on structured low-rank matrix completion. Magn Reson Med 2014;72:959-70.
20. Zhao B, Haldar JP, Brinegar C, Liang ZP. Low Rank Matrix Recovery for Real-Time Cardiac MRI. 2010 IEEE International Symposium on Biomedical Imaging: From Nano to Macro, Rotterdam, Netherlands, 2010:996-9.
21. Aharon M, Elad M, Bruckstein A. K-SVD: An algorithm for designing overcomplete dictionaries for sparse representation. IEEE Transactions on Signal Processing, 2006;54:4311-22.
22. Tsao J, Boesiger P, Pruessmann KP. k-t BLAST and k-t SENSE: dynamic MRI with high frame rate exploiting spatiotemporal correlations. Magn Reson Med 2003;50:1031-42.

23. Liang D, Cheng J, Ke Z, Ying L. Deep Magnetic Resonance Image Reconstruction: Inverse Problems Meet Neural Networks. IEEE Signal Process Mag 2020;37:141-51.
24. Wang G, Ye JC, Mueller K, Fessler JA. Image Reconstruction is a New Frontier of Machine Learning. IEEE Trans Med Imaging 2018;37:1289-96.
25. Liu Q, Yang Q, Cheng H, Wang S, Zhang M, Liang D. Highly undersampled magnetic resonance imaging reconstruction using autoencoding priors. Magn Reson Med 2020;83:322-36.
26. Luo G, Zhao N, Jiang W, Hui ES, Cao P. MRI reconstruction using deep Bayesian estimation. Magn Reson Med 2020;84:2246-61.
27. Tezcan KC, Baumgartner CF, Luechinger R, Pruessmann KP, Konukoglu E. MR Image Reconstruction Using Deep Density Priors. IEEE Trans Med Imaging 2019;38:1633-42.
28. Ke Z, Cheng J, Ying L, Zheng H, Zhu Y, Liang D. An unsupervised deep learning method for multi-coil cine MRI. Phys Med Biol 2020;65:235041.
29. Yaman B, Hosseini SAH, Moeller S, Ellermann J, Uğurbil K, Akçakaya M. Self-supervised learning of physics-guided reconstruction neural networks without fully sampled reference data. Magn Reson Med 2020;84:3172-91.
30. Zhu B, Liu JZ, Cauley SF, Rosen BR, Rosen MS. Image reconstruction by domain-transform manifold learning. Nature 2018;555:487-92.
31. Akçakaya M, Moeller S, Weingärtner S, Uğurbil K. Scan-specific robust artificial-neural-networks for k-space interpolation (RAKI) reconstruction: Database-free deep learning for fast imaging. Magn Reson Med 2019;81:439-53.
32. Eo T, Jun Y, Kim T, Jang J, Lee HJ, Hwang D. KIKI-net: cross-domain convolutional neural networks for reconstructing undersampled magnetic resonance images. Magn Reson Med 2018;80:2188-201.
33. Wang S, Ke Z, Cheng H, Jia S, Ying L, Zheng H, Liang D. DIMENSION: Dynamic MR imaging with both k-space and spatial prior knowledge obtained via multi-supervised network training. NMR Biomed 2022;35:e4131.
34. Kwon K, Kim D, Park H. A parallel MR imaging method using multilayer perceptron. Med Phys 2017;44:6209-24.
35. Han Y, Sunwoo L, Ye JC. k-Space Deep Learning for Accelerated MRI. IEEE Transactions on Medical Imaging 2020;39:377-86.
36. Kofler A, Dewey M, Schaeffter T, Wald C, Kolbitsch C. Spatio-Temporal Deep Learning-Based Undersampling Artefact Reduction for 2D Radial Cine MRI With Limited Training Data. IEEE Trans Med Imaging 2020;39:703-17.
37. Lee D, Yoo J, Tak S, Ye JC. Deep Residual Learning for Accelerated MRI Using Magnitude and Phase Networks. IEEE Trans Biomed Eng 2018;65:1985-95.
38. Mardani M, Gong E, Cheng JY, Vasanawala SS, Zaharchuk G, Xing L, Pauly JM. Deep Generative Adversarial Neural Networks for Compressive Sensing MRI. IEEE Trans Med Imaging 2019;38:167-79.
39. Quan TM, Nguyen-Duc T, Jeong WK. Compressed Sensing MRI Reconstruction Using a Generative Adversarial Network With a Cyclic Loss. IEEE Trans Med Imaging 2018;37:1488-97.
40. Yang G, Yu S, Dong H, Slabaugh G, Dragotti PL, Ye X, et al. DAGAN: Deep De-Aliasing Generative Adversarial Networks for Fast Compressed Sensing MRI Reconstruction. IEEE Trans Med Imaging 2018;37:1310-21.
41. Aggarwal HK, Mani MP, Jacob M. MoDL: Model-Based Deep Learning Architecture for Inverse Problems. IEEE Trans Med Imaging 2019;38:394-405.
42. Hammernik K, Klatzer T, Kobler E, Recht MP, Sodickson DK, Pock T, Knoll F. Learning a variational network for reconstruction of accelerated MRI data. Magn Reson Med 2018;79:3055-71.
43. Hosseini SAH, Yaman B, Moeller S, Hong M, Akçakaya M. Dense Recurrent Neural Networks for Accelerated MRI: History-Cognizant Unrolling of Optimization Algorithms. IEEE J Sel Top Signal Process 2020;14:1280-91.
44. Qin C, Schlemper J, Caballero J, Price AN, Hajnal JV, Rueckert D. Convolutional Recurrent Neural Networks for Dynamic MR Image Reconstruction. IEEE Trans Med Imaging 2019;38:280-90.
45. Qin C, Schlemper J, Duan JM, Seegoolam G, Price A, Hajnal J, Rueckert D. k-t NEXT: Dynamic MR Image Reconstruction Exploiting Spatio-Temporal Correlations. In: Shen D, Liu T, Peters TM, Staib LH, Essert C, Zhou S, Yap PT, Khan A. Medical Image Computing and Computer Assisted Intervention – MICCAI 2019. Lecture Notes in Computer Science(), Springer, 2019;11765:505-13.
46. Sandino CM, Lai P, Vasanawala SS, Cheng JY. Accelerating cardiac cine MRI using a deep learning-based ESPIRiT reconstruction. Magn Reson Med 2021;85:152-67.
47. Schlemper J, Caballero J, Hajnal JV, Price AN, Rueckert D. A Deep Cascade of Convolutional Neural Networks for Dynamic MR Image Reconstruction. IEEE Trans Med Imaging 2018;37:491-503.

48. Yang Y, Sun J, Li H, Xu Z. ADMM-CSNet: A Deep Learning Approach for Image Compressive Sensing. IEEE Trans Pattern Anal Mach Intell 2020;42:521-38.
49. Küstner T, Fuin N, Hammernik K, Bustin A, Qi H, Hajhosseiny R, Masci PG, Neji R, Rueckert D, Botnar RM, Prieto C. CINENet: deep learning-based 3D cardiac CINE MRI reconstruction with multi-coil complex-valued 4D spatio-temporal convolutions. Sci Rep 2020;10:13710.
50. Zhang J, Ghanem B. ISTA-Net: Interpretable Optimization-Inspired Deep Network for Image Compressive Sensing. P Proceedings of the IEEE Conference on Computer Vision and Pattern Recognition (CVPR), 2018:1828-37.
51. Cheng J, Cui ZX, Huang W, Ke Z, Ying L, Wang H, Zhu Y, Liang D. Learning Data Consistency and its Application to Dynamic MR Imaging. IEEE Trans Med Imaging 2021;40:3140-53.
52. Huang W, Ke Z, Cui ZX, Cheng J, Qiu Z, Jia S, Ying L, Zhu Y, Liang D. Deep low-Rank plus sparse network for dynamic MR imaging. Med Image Anal 2021;73:102190.
53. Lyu J, Zhong J, Zhang Z, Zhao L, Xu J, Liu Q, Peng R, Zhang W. Toward single breath-hold whole-heart coverage compressed sensing MRI using VAriable spatial-temporal LAtin hypercube and echo-Sharing (VALAS). ISMRM 2019:abstr 4752.
54. Berg CA, Larsson EM, Arheden H, Hedström E. Accelerated imaging of the heart using SENSE. ISMRM 2008:1859.
55. Otazo R, Candès E, Sodickson DK. Low-rank plus sparse matrix decomposition for accelerated dynamic MRI with separation of background and dynamic components. Magn Reson Med 2015;73:1125-36.
56. Uecker M, Lai P, Murphy MJ, Virtue P, Elad M, Pauly JM, Vasanawala SS, Lustig M. ESPIRiT--an eigenvalue approach to autocalibrating parallel MRI: where SENSE meets GRAPPA. Magn Reson Med 2014;71:990-1001.
57. Zhan YB, Zhang R. No-Reference Image Sharpness Assessment Based on Maximum Gradient and Variability of Gradients. IEEE Transactions on Multimedia 2018;20:1796-808.
58. Yan X, Luo Y, Chen X, Chen EZ, Liu Q, Zou L, Bao Y, Huang L, Xia L. From Compressed-Sensing to Deep Learning MR: Comparative Biventricular Cardiac Function Analysis in a Patient Cohort. J Magn Reson Imaging 2024;59:1231-41.
59. Wu X, Tang L, Li W, He S, Yue X, Peng P, Wu T, Zhang X, Wu Z, He Y, Chen Y, Huang J, Sun J. Feasibility of accelerated non-contrast-enhanced whole-heart bSSFP coronary MR angiography by deep learning-constrained compressed sensing. Eur Radiol 2023;33:8180-90.
60. Lin L, Li Y, Wang J, Cao L, Liu Y, Pang J, An J, Jin Z, Wang Y. Free-breathing cardiac cine MRI with compressed sensing real-time imaging and retrospective motion correction: clinical feasibility and validation. Eur Radiol 2023;33:2289-300.
61. Zucker EJ, Sandino CM, Kino A, Lai P, Vasanawala SS. Free-breathing Accelerated Cardiac MRI Using Deep Learning: Validation in Children and Young Adults. Radiology 2021;300:539-48.
62. Kido T, Kido T, Nakamura M, Watanabe K, Schmidt M, Forman C, Mochizuki T. Compressed sensing real-time cine cardiovascular magnetic resonance: accurate assessment of left ventricular function in a single-breath-hold. J Cardiovasc Magn Reson 2016;18:50.

Cite this article as: Yan C, Liu Y, Wang C, Fan W, Zhu Y. Accelerated cardiac cine magnetic resonance imaging using deep low-rank plus sparse network: validation in patients. Quant Imaging Med Surg 2024;14(7):5131-5143. doi: 10.21037/qims-24-17

